Bending and Collapse: Magnetic Recording Fidelity of Magnetofossils from Micromagnetic Simulation

Bending and Collapse: Magnetic Recording Fidelity of Magnetofossils from Micromagnetic Simulation

Zhaowen Pei[1], Thomas A. Berndt[2*], Liao Chang[1,3*], Fan Bai[1], Wyn Williams[4], and Greig A. Paterson[5]

[1]Laboratory of Orogenic Belts and Crustal Evolution, School of Earth and Space Sciences, Peking University, Beijing 100871, PR China

[2]Department of Geophysics, School of Earth and Space Sciences, Peking University, Beijing 100871, PR China

[3]Laboratory for Marine Geology, Qingdao National Laboratory for Marine Science and Technology, Qingdao 266071, PR China

[4]Earth and Planetary Science, School of Geosciences, University of Edinburgh, Edinburgh EH9 3FE, UK

[5]Department of Earth, Ocean and Ecological Sciences, University of Liverpool, Liverpool, L697ZE, UK

[*]Corresponding author: T. A. Berndt (thomasberndt@pku.edu.cn), L. Chang (liao.chang@pku.edu.cn)

Key Points:

- Hysteresis parameters can be used to estimate the collapse degree of magnetofossil chains.
- Micromagnetic calculations confirm that collapsed magnetofossils retain their primary paleomagnetic signal.
- Magnetic remanence carried by magnetofossils remains thermally stable over long geological time.

This article has been accepted for publication and undergone full peer review but has not been through the copyediting, typesetting, pagination and proofreading process, which may lead to differences between this version and the Version of Record. Please cite this article as doi: 10.1029/2021JB023447.

Abstract

Magnetosome chains produced by magnetotactic bacteria are important paleoenvironmental and paleomagnetic recorders. It has been shown that magnetic properties of magnetosome chains are closely related to their morphology and chain structures; however, the *in-situ* structures of magnetosome chains in sediments (magnetofossils) are not known. Magnetosome chains are subject to various deformations after cell dissolution and are therefore unlikely to be fully intact, obscuring their original magnetic signals. Here we use finite element micromagnetic simulations to quantify changes in magnetic signals in response to chain deformation, in particular, as a function of variable degrees of bending and collapse. Our results indicate that bending/collapse leads to a significant coercivity reduction and domain state transition of the chain. Therefore, hysteresis parameters can be used to assess the degree of chain bending/collapse in magnetofossil-rich sediments. Calculations of the contributions of chain bending/collapse to the post-depositional remanent magnetization (pDRM) of magnetofossils indicate that pDRM remains both faithful to the pre-bending/collapse natural remanent magnetization, and that the remanence of some structurally deformed magnetofossil assemblages remains thermally stable over billion-year timescales, suggesting that even strongly deformed magnetosome chains in ancient geological materials retain faithful paleomagnetic records and thus have potentials for tracing ancient geomagnetic field variations and microbial activities on early Earth.

Plain Language Summary

Magnetotactic bacteria (MTB) synthesize magnetosome chains composed of nearly uniform magnetic nanoparticles (magnetite or greigite). Magnetosomes can be preserved as magnetofossils in sediments after MTB cell death, which work as a magnetic tape to encode critical signals about past geomagnetic field variations, environmental changes, and microbial

activities. However, these geophysical signals may likely be corrupted due to potential chain collapse during sediment deformation, which complicates signal recovery. Here we used computer simulation to calculate the magnetic signal variations of magnetofossils related to chain bending or collapse. Our simulations suggest that collapsed magnetofossils can still retain faithful paleomagnetic signals that are stable over very long geological periods. This approach also provides a framework for estimating the chain collapse degree that is critical for magnetic signal interpretation.

1. Introduction

Magnetosomes synthesized by magnetotactic bacteria (MTB) are membrane bound magnetic mineral crystals, either magnetite or greigite, arranged in chains with specific morphologies and narrow size ranges (Bazylinski & Frankel, 2004). Magnetosomes can be preserved in sediments as magnetofossils (Kopp & Kirschvink, 2008), which are considered to be excellent paleomagnetic recorders, routinely used for magnetostratigraphic dating (e.g., Channell et al., 2013; Larrasoaña et al., 2014; Roberts et al., 2013), relative paleointensity determination (e.g., Chen et al., 2017; Roberts et al., 2012; Yamazaki & Yamamoto, 2018), and paleoenvironmental reconstructions (e.g., Chang et al., 2018; Roberts et al., 2011; Yamazaki, 2012).

Magnetosome chains in living MTB cells are usually straight or slightly bent (Orue et al., 2018). Physical calculations considering elastic and magnetic forces showed that magnetosome chains can kink due to magnetic interaction under strong external forces (Shcherbakov et al., 1997). Other calculations showed that ring structure is the lowest energy configuration for magnetosome chains without a stabilizing filament structure (Kiani et al., 2015, 2018). Moreover, folded chains and flux-closure rings have been observed in attempts to create

colloidal magnetosome suspensions (Philipse and Maas, 2002). It is likely that magnetofossils in sediments are not preserved in their original intact structures after a range of complex sedimentary processes that can cause magnetosome chains to bend or collapse; for example, during settlement through the water column in profundal facies (Lascu & Plank, 2013) and post-depositional sedimentary diagenesis (McNeill & Kirschvink, 1993). Furthermore, magnetic mineral dissolution caused by diagenesis may affect magnetofossil preservation (Roberts, 2015). Bacterial culture experiments (Kobayashi et al., 2006; Li et al., 2012) and numerical simulations (Amor et al., 2022; Chang et al., 2019; Harrison & Lascu, 2014) revealed that the degree of bending or collapse significantly affects rock magnetic properties of magnetosome chains. However, the *in-situ* magnetofossil chain structures in sediments have not been reported. A careful rock magnetic investigation of magnetofossil-rich sediments suggested an upper limit of the magnetofossil concentration at ~0.14% by volume and typical distances between chains of >9 times their length (Ludwig et al., 2013). This means that MTB cells were originally separated by sediments matrices, and that chain clumping after cell dissolution did not occur, unlike results from chain disruption experiments using bacterial cultures (e.g., Kopp et al., 2006; Li et al., 2012). Moreover, magnetosome chains may adhere to the surfaces of clay minerals in sediments (Galindo-Gonzalez et al., 2009), thereby stabilizing the chain structure. Since the *in-situ* chain structures are unknown, we carry out systematical forward modeling to explore the effect of two possible modes of chain structure deformation on their magnetic properties in sediments: a regular bending model from straight chains to rings, and a random-walk collapse model.

Early studies have shown that magnetofossils can acquire natural remanent magnetization (NRM) through two possible mechanisms: (1) If magnetosome chains aligning with the geomagnetic field maintain their orientation after MTB death, magnetofossils can acquire a

biogeochemical remanent magnetization (BgRM; Abrajevitch & Kodama, 2009; Tarduno et al., 1998); (2) If magnetosome chains reorient due to the geomagnetic field in the water column or through other forces (e.g., bioturbation and compaction) during sedimentary processes after MTB death, magnetofossils can acquire a depositional (or post-depositional) remanent magnetization (DRM or pDRM; Heslop et al., 2013). Chain bending/collapse may occur during sedimentary compaction, possibly leading to magnetofossils acquiring pDRM that could obscure an earlier natural remanent magnetization (NRM). Furthermore, chain collapse may also reduce the paleomagnetic stability of any remanent magnetization, thereby losing any NRM altogether. However, these effects have not been quantitatively assessed, and hence, the paleomagnetic reliability and stability of bent or collapsed magnetofossil chains over geological times are currently unclear.

Biogenic magnetite has the potential of being used as a paleoenvironmental indicator due to the responsiveness of MTB and their biosynthesized magnetic particles to environmental conditions (e.g., Chang et al., 2018; Roberts et al., 2011; Yamazaki, 2012; Yamazaki & Kawahata, 1998). Hysteresis properties are fast and easy to measure and potentially allow to infer types and amounts of magnetosomes in sediments, which can be used as a magnetic paleoenvironmental proxy (e.g., Berndt et al., 2020; Chang et al., 2018; Egli, 2004). While hysteresis parameters at least partially depend on the size and shape of biogenic particles, i.e., factors controlled by the paleoenvironment, micromagnetic simulations in FORCulator indicate that magnetic hysteresis properties of magnetosomes are sensitive to chain structures (Chang et al., 2019; Harrison & Lascu, 2014). However, the point dipole approximation by FORCulator neglects – and hence cannot predict – particle dimensions. Recently, a systematic extensive three-dimensional finite-element micromagnetic simulation was performed to establish the

relationship between hysteresis properties and both particle and chain morphology (i.e., magnetosome size, elongation, intra-chain spacing, and chain length) of straight magnetosome chains (Berndt et al., 2020). Here, we extend this model to bent and collapsed magnetofossils to address two key questions: (1) How does chain bending/collapse affect magnetic hysteresis parameters (which are routinely used in paleoenvironmental studies)? (2) Is any pDRM carried by bending/collapse chain faithful to the pre-collapse/bending NRM (i.e., in the same direction and with a proportional intensity), and thermally stable over geological timescales?

We generated more than 200 magnetosome models with variable degrees of chain bending and collapse, and calculated hysteresis loops, back-field curves, and first-order reversal curves (FORC). We also simulated pDRM after chain collapse/bending and calculated blocking temperatures to assess the paleomagnetic recording reliability of magnetofossil assemblages in sediments and sedimentary rocks.

2. Methods

2.1. Micromagnetic models

Two types of geometrical models were built: (1) a bending model where the chain forms a regular arc (Figure 1a-1b), and (2) a collapse model (Figures 1c-1d), where particles follow a three-dimensional random-walk (Harrison & Lascu, 2014). All models contain 10 cubic or cuboctahedral particles spaced at an inter-particle spacing d and forming a bending angle b or collapse angle c. Based on a grain size analysis of magnetosomes from transmission electron microscopic (TEM) images (Berndt et al., 2020), we chose only the most common crystal sizes for modeling, including equant and elongated (with an aspect ratio of 1.2) 40 nm grains with tight (i.e., d = 3 nm) and loose (i.e., d = 8 nm) inter-particle spacing, as well as tightly spaced

(i.e., d = 3 nm), equant 100 nm particles (Table 1). The center angle formed by 10 particles arranged in a complete ring is 324°, so regular bending angles ranging from 0° to 324° with a step size of 30° were modeled. We modeled collapse angles in the range of 0° to 70° with a step size of 10° (since higher bending degrees cause overlapping of particles). Ten random-walk collapse models were generated for each collapse angle.

The models were meshed with the finite-element software Trelis 16.3 (Trelis, 2021) with a mesh size of 9 nm. Micromagnetic simulations were done in finite element micromagnetic modeling package MERRILL version 1.3.5 (Ó Conbhuí et al., 2018). The cubic anisotropy axes of all particles in a chain were rotated with the corresponding bending/collapse angles to align with the chain axis. Simulation results were visualized using ParaView 5.5.2 (Ahrens et al., 2005).

2.2. Hysteresis simulations

As hysteresis loops of magnetosome chains depend strongly on applied field direction (Li et al., 2013), we use 100 random field directions (in 3D space) for 40 nm bending models, 25 for 100 nm bending models, 10 for 40 nm collapse models, and 5 for 100 nm collapse models due to the limitation of computing time (Table S1). The applied field ranges from –300 mT to +300 mT with a step size of 1 mT at low fields (0-5 mT), 5 mT at medium fields (5-100 mT), and 20 mT at high fields (>100 mT). The same random magnetic field directions were used for the back-field curve calculations, as follows: (1) calculating the saturation remanence with a positive 300 mT saturation field, (2) applying fields from 5 mT to 300 mT successively in the negative field direction and obtaining remanence at each field step. The step size is -5 mT from -5 mT to -100 mT and -20 mT from -100 mT to -300 mT. The same particle size (i.e., 40 nm) and crystalline forms (i.e., cuboctahedra) and 100 random field directions were used for FORC simulation. The

applied field ranges from –200 mT to +200 mT with a step size of 2 mT. We used 100 random field directions to simulate FORCs for straight and bending models. 20 random-walk collapse models were established for each collapse angle and FORCs in 20 random external magnetic field directions were simulated.

2.3. pDRM simulations

To investigate the paleomagnetic reliability and stability of bent or collapsed magnetofossils over geological times, an initially straight chain with a saturation remanent magnetization state (SIRM; i.e., the pre-collapse/bending NRM) was progressively bent/collapsed in steps of 30°/10°, respectively. Then, the magnetic moment vectors at all vertices of the mesh were rotated and loaded into the model with the next higher bending angle. Next, the energy of this magnetic state was re-minimized in zero field to obtain the magnetic state. The magnetization calculated at each step is used to simulate pDRM with increasing bending or collapse angle. Moreover, the effect of changes in pDRM intensity relative to straight chains due to the geometric rotation of magnetic moments in each particle was calculated analytically. If the pDRM was perfectly faithful to the pre-collapse/bending NRM, the new state should be identical to a purely geometric rotation of all magnetic moments; if on the other hand, a change in the domain state of the chain or individual grain occurs, the initial NRM signal can become corrupted. Similarly, we simulated pDRM in the same random directions as hysteresis simulations.

Energy barriers between two local energy minima (LEM) states can be calculated in MERRILL using the Nudged–elastic-band (NEB) method, which can determine the minimum energy transition between two given LEM states (Nagy et al., 2017; Ó Conbhuí et al., 2018). Considering that the particles in our chain model have strong interaction, we regard the chain as

a single system for the NEB calculations. When calculating the minimum energy path, we set two antiparallel stable remanent states along the chains, generated in the above pDRM simulations as two endpoints. Energy barriers between two antiparallel endpoints were calculated to obtain the thermal stability of the pDRM. Moreover, we calculated the energy of 100 random minimized magnetization states to check whether there are any other possible stable states and whether the chain-aligned remanence state has the lowest energy.

The NEB method for calculating energy barriers using the constraint of minimum action (Fabian & Scherbakov, 2018) requires that there should be no intermediate minima between the LEM endpoints. For the energy paths with obvious intermediate minima, we extracted these intermediate minimum states as the new endpoint to split the path, and then recalculated the minimum energy paths until there are no intermediate minima in the new paths. From these splitting paths, we chose those that provided the lowest energy barrier to calculate the relaxation time τ (Nagy et al., 2017; Néel, 1949). The T_B was then calculated by repeating the calculation at multiple temperatures up to just below the Curie temperature and selecting the temperature where the relaxation time is of the order of minutes (i.e., τ = 100 s; Nagy et al., 2017).

We calculated minimum energy paths of some typical magnetosome chain models at different temperatures using the NEB method (Figure S1). These minimum energy paths contain fewer intermediate minima at high temperatures (500 °C) compared to lower temperatures (< 400 °C; Figure S1), reflecting the increased path stability as the magnetostatic interactions, which is proportional to the saturation magnetization decrease with temperature. Minimum energy paths of straight chain model (b = 0°) do not contain intermediate minima at 500 °C (Figure S1d). Minimum energy paths of a ring-shaped model (b = 324°) and a medium collapse model (c = 30°) have only one obvious intermediate minimum at 500 °C (Figures S1l and S1p). Minimum

energy paths of a strong collapse model (c = 70°) have two obvious minima at 400 ℃ and 500 ℃ (Figures S1s-S1t). Only the minimum energy paths of a bending model (b = 180°) still contain much noise at high temperatures (Figures S1g-S1h). Hence, we chose straight chain model, ring-shaped model, 30° collapse model, and 70° collapse model to calculate energy barriers at high temperature ranges using path splitting method. Then, we used polynomial fitting to estimate their blocking temperature (Nagy et al., 2017).

3. Results

3.1. Hysteresis loops and back-field curves

Our simulations of hysteresis loops (Figure S2) and back-field curves (Figure S3) show that both the coercivity (B_c) and the coercivity of remanence (B_{cr}) decrease gradually by about 50% with progressive bending/collapse angle for completely bent/collapsed chains (Figures 2a-2d). The ratio of saturation remanence to saturation magnetization (M_{rs}/M_s) increases slightly from 0.5 (the theoretical value for uniaxial particles) to ~0.6 for 40 nm bending model, indicating a deviation from perfect uniaxiality, but decreases significantly for the 40 nm collapse model (Figures 2e-2f). However, both bent and collapsed 100 nm models have strongly decreasing values (Figures 2e-2f), because the domain states of the individual particles switch from single domain (SD) to single-vortex (SV) with increasing bending/collapse angle.

Hysteresis loops of bent and collapsed magnetofossils differ from those of straight chains, which only have one major switch (Berndt et al., 2020): Chains with large bending angles can switch twice (Figure 3), while strongly collapsed chains can switch multiple times (Figure 4). For strongly bent chains, which are almost circular, the first switching is characterized by domain alignment approximately along the chain direction (i.e., from ① to ② in Figure 3); the

second switching corresponds to domain alignment along the external field direction (i.e., from ③ to ④ in Figure 3). These two switches manifest as two distinct jumps in a hysteresis loop (Figure 3). Collapse models may have multiple switches, leading to segmented jumps in the hysteresis loop (e.g., Figure 4).

Saturation remanent states of grains in all 40 nm bending and collapse magnetosome models exhibit SD behavior, but show multiple orientations of magnetic moments: (1) Similar to straight chains (Berndt et al., 2020), moment directions in slightly bent models are parallel to the chain axis in all directions of external fields (Figures 5a, 5c); (2) Some moments in strongly bent chains are perpendicular to the chain axis when the external field direction is perpendicular to the chain (Figure 5b); (3) Collapsed chains have multiple magnetic moment directions depending on chain structures (Figure 5e). Particles at both ends of 100 nm chains with slight bending are in SV states (Figure 5c), but all particles in a chain are in SV states for 100 nm models with strong bending (Figures 5d, f).

3.2. FORC diagrams

Simulations reveal a significant effect of bending and collapse on FORC diagrams. Straight chains show the typical central ridge in FORC diagrams, along with a negative distribution in the lower-left region due to reversible magnetization of randomly oriented chains (Figure 6a; Chang et al., 2019; Harrison & Lascu, 2014; Newell, 2005). FORC diagrams of ring-shaped models (b = 300°) contain three distinct peaks (Figure 6b), which is due to transient behavior of the nucleation and annihilation of the super-vortex that spans the entire ring (Carvallo et al., 2003; Zhao et al., 2017). Similarly, collapse leads to a shift of the central ridge towards lower coercivities along with a vertical broadening of the signal (c = 30°, Figure 6c) and eventually to the formation of 'wings' similar to those caused by an increase of the 3D

interaction fields (c = 60°, Figure 6d).

3.3. Contributions of bending/collapsed chains to pDRM and their thermal stability

When magnetofossil chains are bent/collapsed during deposition, the magnetic remanence is reduced due to (1) the geometric rotation of particles away from the original deposition axis, and (2) changes in domain states of either individual particle or the whole chain. Our models show that the reduction of pDRM intensity in a single chain due to bending/collapse can almost entirely be explained by the geometrical rotation of particles, which leads to 100% and 60 % reduction for ring-shaped and fully collapsed chains respectively (Figures 7a-7b and S4a). For the 40 nm models, their magnetic states are always SD and are consistent with the geometric bending/collapse direction (Figures 8a, 8c, and 8e). Only the 100 nm models deviate slightly from this, which is because the domain states change from SD to SV for the 100 nm particles with increasing bending or collapse (Figures 8b, 8d, 8f). Simulated change in the normalized pDRM intensity (pDRM/SIRM) for deformed chains relative to straight chains gradually decreases to zero with increasing bending degree (Figures 7c and S4c), but first increase slightly and then decrease continuously for collapse angle > ~20° (Figures 7d), which is caused by the relatively faster SIRM decrease with collapse than the pDRM for collapse model (Figures 2f and 7b).

Simulation results show that the magnetization states with magnetic moment aligned along the chain (i.e., endpoint states in our study) are the lowest energy states (Figure S5). There are some other possible stable magnetization states, but their energy is higher than that of chain-aligned states (Figure S5), indicating that they are probably local minimization states, not global energy minimum states.

The straight chain model without an intermediate minimum has a high energy barrier at 500℃ (Figure 9a) and we determined a high T_B of 549 ℃ (Figure 11). The minimum energy paths calculated by splitting at intermediate minima are basically consistent with original energy paths for the ring-shaped model and two collapse models (Figures 9b and 10). The T_B of ring-shaped model, 30° collapse model, and 70° collapse model are 551 ℃, 519 ℃, and 354 ℃, respectively (Figure 11). Therefore, chain collapse does lead to a reduction in T_B, but it still remains high enough to be stable over geological time scales. Hence, these four models with different chain structures have high T_B, indicating the high thermal stability of magnetosome chain remanence.

4. Discussion

4.1. Assessing collapse degree from rock magnetic properties

Our simulations indicate that bending and collapse significantly affects the magnetic properties of magnetosome chains, especially the reduction of coercivity (Figures 2a-2d), which is consistent with previous micromagnetic simulations (Chang et al., 2019; Harrison & Lascu, 2014) and experimental data (Kobayashi et al., 2006; Li et al., 2012). A change in the structure of the interaction fields, which become less aligned in the chain direction, leads to the reduction of coercivity through a number of effects. First, the external magnetic field is at an angle to the magnetization so that the magnetostatic interaction energy is reduced. Furthermore, particle gaps in a chain increase with increasing bending and collapse, and therefore significantly reduce coercivity (Berndt et al., 2020). Moreover, a gradual increase in bending or collapse degree disrupts the ordered chain arrangement in the chain direction, which makes it easier for

individual grains to switch their magnetization, resulting in multiple switching in some chains (Figures 3-4), hence, reducing the coercivity.

Currently, it is difficult to directly quantify magnetosome chain structures within sediment samples. Extracted magnetofossil assemblages imaged by electron microscope observations do not represent their *in-situ* microstructures in sediments due to deformation of chain structures during sample preparation. Some studies proposed to evaluate the bending or collapse degree of magnetosome chains using comprehensive rock magnetic parameters. It has been shown that collapse of magnetosome chains lowers the ratio of anhysteretic remanent magnetization (ARM) susceptibility to saturation isothermal remanent magnetization (χ_{ARM}/SIRM; Lascu & Plank, 2013; Li et al., 2012), and produces a lower delta ratio between losses of field cooled (FC) and zero-field cooled (ZFC) remanent magnetization across the Verwey transition in low-temperature experiments (δ_{FC}/δ_{ZFC}; Carter-Stiglitz et al, 2002; Li et al., 2012).

Here, we propose a simple strategy to estimate chain collapse from hysteresis experiments of magnetofossil-dominated samples. Our simulations show that data of collapse models move significantly to the lower-left region with progressive collapse angle in the Néel diagram (Néel, 1955; Figure 12). Previous experimental data show a consistent trend (Figure 12): Intact magnetosome chains in MTB have a ratio of ~0.5 and higher coercivity (25-40 mT; Jovane et al., 2012; Li et al., 2012; Lin & Pan, 2009; Moskowitz et al., 1988; Pan et al., 2005), but collapsed and clumped chains from culture experiments have a lower M_{rs}/M_s ratio (the lowest ratio is close to 0.2) and coercivity (even less than 10 mT; Li et al., 2012). Some magnetofossil-rich sediments have similar M_{rs}/M_s ratio and coercivity to the medium and strong collapse model (Figure 12; Chang et al., 2018; Ludwig et al., 2013), indicating that magnetosome chains in

natural samples may have medium to high collapse angles. In addition, data of bending models move sightly to the upper-left region with progressive bending angle in the Néel diagram (Figure S6). In particular, the M_{rs}/M_s ratio of ring-shaped chain reaches ~0.6, which is different from data trend of bacterial culture experiments and natural sediment samples. Hence, we speculate that while slight bending occurs in magnetosome chains in intact MTB cells, magnetofossils in compacted sediments are unlikely to experience such a systematic bending. Rather, the chain collapse model is more likely to be representative of deformed magnetofossils in sediments than the regular bending model. Furthermore, our simulations reveal that FORC distributions are also sensitive to chain bending and collapse (Figure 6). However, these results are obtained by forward simulation of pure magnetosome chains. It is necessary to consider the influence of magnetic minerals of other origins in sediments on the bulk magnetic properties. Therefore, we can first separate the magnetofossil component using magnetic unmixing techniques such as isothermal remanent magnetism curves (Egli, 2004), central ridge analysis of FORC diagrams (Egli et al., 2010), or FORC-principal component analysis (FORC-PCA; Harrison et al., 2018; Lascu et al., 2015). Then, it is possible to use the Néel diagram and FORC diagrams to qualitatively evaluate chain collapse in natural magnetofossil-dominated samples based on our forward simulation.

4.2. Paleomagnetic recording fidelity of collapsed magnetofossils

Magnetofossils can effectively acquire NRM in suitable depositional environments (Mao et al., 2014; Paterson et al., 2013) and can dominate the NRM in some sediments (Heslop et al., 2013). However, magnetofossils may acquire pDRM through chain bending/collapse during sedimentary processes. Our simulation results indicate that the pDRM intensity contributed by magnetofossils is sensitive to the degree of chain bending and collapse (Figures 7a-7d).

Importantly, however, our micromagnetic and analytical calculations indicate that the geometry of particle rotation – rather than changes in domain state – is the major cause of pDRM reduction in collapsed magnetosome chains (Figures 7a-7b), indicating that pDRMs are faithful to the pre-collapse/bending NRM, albeit with a weaker intensity. Therefore, we can first obtain the magnetofossil concentrations in sediments using rock magnetic unmixing techniques, and then changes in relative paleointensity due to collapse can be corrected if the chain collapse degree in magnetofossil-dominated sediments can be evaluated.

Biomineralization of magnetosomes in bacteria is thought to have existed for a long time in geological history (Lin et al., 2017, 2018, 2020) with the earliest geological evidence of magnetofossils having an age of ~2 Ga (Chang & Kirschvink, 1989). Despite the billion-year timescales of remanences carried by collapsed magnetofossil chains, our simulations suggest that even some strongly bent or collapsed magnetosomes have high blocking temperatures and are capable of retaining stable remanence over geological timescales. Hence, although the pDRM is weakened by post-depositional processes, magnetofossils in ancient rocks can still effectively preserve the palaeomagnetic fields of the early Earth.

5. Conclusions

Our quantitative micromagnetic simulations indicate that bending and collapse of magnetosome chains have a strong effect on rock magnetic properties and paleomagnetic records of magnetofossil-bearing samples, with apparent coercivity reductions, transition in the domain state of the whole chain, and pDRM intensity reductions with increasing bending or collapse. More importantly, our simulations of blocking temperature indicate that bent or collapsed magnetosome chains can retain a stable pDRM over billion-year timescales. We also show that pDRMs are not only stable but also faithful to the pre-collapse/bending NRM, both in direction

and in intensity through a simple geometric reduction in magnitude. The collapse degree of chains can be estimated qualitatively from Néel diagram and FORC diagrams, which may allow correction of the reduction in paleointensity of magnetofossil-dominated samples due to chain collapse. Our simulation provides new quantitative constraints on understanding the magnetic signatures of magnetofossils, which are important for reconstructing paleoenvironmental conditions and geomagnetic field variations.

Acknowledgments

This study was supported by the National Natural Science Foundation of China (NSFC grant 41974074) to L.C. and T.A.B. L.C. acknowledges additional support from the NSFC (grants 42061130214, 41722402) and a Royal Society-Newton Advanced Fellowship (NAF\R1\201096). Z.P. acknowledges an undergraduate research Junzheng grant from Peking University. W.W. would like to acknowledge support from the Natural Environmental Research Council (NERC) through grants NE/T000473/1 and NE/S011978/1. G.A.P. is supported by a NERC Independent Research Fellowship (NE/P017266/1). We thank Editor Mark Dekkers for efficient editorial handling, and Associate Editor Adrian Muxworthy, Ramon Egli, and Xiang Zhao for providing constructive comments that improved this paper.

Data Availability Statement

The complete source code used to produce the data is available on https://doi.org/10.5281/zenodo.5881792. The calculated hysteresis data and energy barriers data are available on the Peking University Open Research Data Platform (https://doi.org/10.18170/DVN/P7KDKR).

References

Abrajevitch, A., & Kodama, K. (2009). Biochemical vs. detrital mechanism of remanence

acquisition in marine carbonates: A lesson from the K–T boundary interval. *Earth and Planetary Science Letters*, 286(1), 269–277. https://doi.org/10.1016/j.epsl.2009.06.035

Ahrens, J., Geveci, B., & Law, C. (2005). ParaView: An end-user tool for large-data visualization. In C. D. Hansen, & C. R. Johnson (Eds.), *The visualization handbook* (pp. 717–731). Elsevier. https://doi.org/10.1016/B978-012387582-2/50038-1

Amor, M., Wan, J., Egli, R., Carlut, J., Gatel, C., Andersen, I. M., Snoeck, E., & Komeili, A. (2021). Key signatures of magnetofossils elucidated by mutant magnetotactic bacteria and micromagnetic calculations. *Journal of Geophysical Research: Solid Earth*, e2021JB023239, https://doi.org/10.1029/2021JB023239

Bazylinski, D. A., & Frankel, R. B. (2004). Magnetosome formation in prokaryotes. *Nature Reviews. Microbiology, 2*(3), 217–230. https://doi.org/10.1038/nrmicro842

Berndt, T. A., & Chang, L. (2019). Waiting for forcot: Accelerating FORC processing 100× using a fast-fourier-transform algorithm. *Geochemistry, Geophysics, Geosystems, 20*, 6223–6233. https://doi.org/ 10.1029/2019GC008380

Berndt, T. A., Chang, L., & Pei, Z. (2020). Mind the gap: Towards a biogenic magnetite palaeoenvironmental proxy through an extensive finite-element micromagnetic simulation. *Earth and Planetary Science Letters, 532*, 116010. https://doi.org/10.1016/j.epsl.2019.116010

Carter-Stiglitz, B., Jackson, M., & Moskowitz, B. (2002). Low-temperature remanence in stable single domain magnetite. *Geophysical Research Letters, 29*(7), 1129. https://doi.org/10.1029/2001GL014197

Carvallo, C., Muxworthy, A. R., Dunlop, D. J., & Williams, W. (2003). Micromagnetic modeling of first-order reversal curve (FORC) diagrams for single-domain and pseudo-

single-domain magnetite. *Earth and Planetary Science Letters, 213*(3–4), 375–390. https://doi.org/10.1016/S0012-821X(03)00320-0

Chang, L., Harrison, R. J., & Berndt, T. A. (2019). Micromagnetic simulation of magnetofossils with realistic size and shape distributions: Linking magnetic proxies with nanoscale observations and implications for magnetofossil identification. *Earth and Planetary Science Letters, 527*, 115790. https://doi.org/10.1016/j.epsl.2019.115790

Chang, L., Harrison, R. J., Zeng, F., Berndt, T. A., Roberts, A. P., Heslop, D., & Zhao, X. (2018). Coupled microbial bloom and oxygenation decline recorded by magnetofossils during the Palaeocene–Eocene thermal maximum. *Nature Communications, 9*(1), 4007–9. https://doi.org/10.1038/s41467-018-06472-y

Channell, J. E. T., Ohneiser, C., Yamamoto, Y., & Kesler, M. S. (2013). Oligocene-miocene magnetic stratigraphy carried by biogenic magnetite at sites U1334 and U1335 (equatorial pacific ocean). *Geochemistry, Geophysics, Geosystems, 14*(2), 265–282. https://doi.org/10.1029/2012GC004429

Chen, L., Heslop, D., Roberts, A. P., Chang, L., Zhao, X., McGregor, H. V., Marino, G., Rodriguez-Sanz, L., Rohling, E. J., & Pälike, H. (2017). Remanence acquisition efficiency in biogenic and detrital magnetite and recording of geomagnetic paleointensity. *Geochemistry, Geophysics, Geosystems, 18*(4), 1435–1450. https://doi.org/10.1002/2016GC006753

Chang, S. B. R., & Kirschvink, J. L. (1989). Magnetofossils, the magnetization of sediments, and the evolution of magnetite biomineralization. *Annual Review of Earth and Planetary Sciences, 17*(1), 169–195. https://doi.org/10.1146/annurev.ea.17.050189.001125

Egli, R. (2004). Characterization of individual rock magnetic components by analysis of

remanence curves, 1. Unmixing natural sediments. *Studia Geophysica et Geodaetica, 48*(2), 391–446. https://doi.org/10.1023/B:SGEG.0000020839.45304.6d

Egli, R., Chen, A. P., Winklhofer, M., Kodama, K. P., & Horng, C. S. (2010). Detection of noninteracting single domain particles using first-order reversal curve diagrams. *Geochemistry, Geophysics, Geosystems, 11*(1), Q01Z11. https://doi.org/10.1029/2009GC002916

Fabian, K., & Shcherbakov, V. P. (2018). Energy barriers in three-dimensional micromagnetic models and the physics of thermoviscous magnetization. *Geophysical Journal International, 215*(1), 314–324. https://doi.org/10.1093/gji/ggy285

Galindo-Gonzalez, C., Feinberg, J. M., Kasama, T., Cervera Gontard, L., Pósfai, M., Kósa, I., Duran, J. D. G., Gil, J. E., Harrison, R. J., & Dunin-Borkowski, R. E. (2009). Magnetic and microscopic characterization of magnetite nanoparticles adhered to clay surfaces. *American Mineralogist, 94*(8-9), 1120–1129. https://doi.org/10.2138/am.2009.3167

Harrison, R. J., & Lascu, I. (2014). FORCulator: A micromagnetic tool for simulating first-order reversal curve diagrams. *Geochemistry, Geophysics, Geosystems, 15*(12), 4671–4691. https://doi.org/10.1002/2014GC005582

Harrison, R. J., Muraszko, J., Heslop, D., Lascu, I., Muxworthy, A. R., & Roberts, A. P. (2018). An improved algorithm for unmixing first-order reversal curve diagrams using principal component analysis. *Geochemistry, Geophysics, Geosystems, 19*(5), 1595–1610. https://doi.org/10.1029/2018GC007511

Heslop, D., Roberts, A. P., Chang, L., Davies, M., Abrajevitch, A., & De Deckker, P. (2013). Quantifying magnetite magnetofossil contributions to sedimentary magnetizations. *Earth and Planetary Science Letters, 382*, 58–65. https://doi.org/10.1016/j.epsl.2013.09.011

Jovane, L., Florindo, F., Bazylinski, D. A., & Lins, U. (2012). Prismatic magnetite magnetosomes from cultivated magnetovibrio blakemorei strain MV-1: A magnetic fingerprint in marine sediments? *Environmental Microbiology Reports, 4*(6), 664-668. https://doi.org/10.1111/1758-2229.12000

Kiani, B., Faivre, D., & Klumpp, S. (2015). Elastic properties of magnetosome chains. *New Journal of Physics, 17*, 043007. https://doi.org/10.1088/1367-2630/17/4/043007

Kiani, B., Faivre, D., & Klumpp, S. (2018). Self-organization and stability of magnetosome chains — A simulation study. *PLOS One, 13*(1), e0190265. https://doi.org/10.1371/journal.pone.0190265

Kobayashi, A., Kirschvink, J. L., Nash, C. Z., Kopp, R. E., Sauer, D. A., Bertani, L. E., Voorhout, W. F., & Taguchi, T. (2006). Experimental observation of magnetosome chain collapse in magnetotactic bacteria: Sedimentological, paleomagnetic, and evolutionary implications. *Earth and Planetary Science Letters, 245*(3-4), 538–550. https://doi.org/10.1016/j.epsl.2006.03.041

Kopp, R. E., & Kirschvink, J. L. (2008). The identification and biogeochemical interpretation of fossil magnetotactic bacteria. *Earth-Science Reviews, 86*(1), 42–61. https://doi.org/10.1016/j.earscirev.2007.08.001

Kopp, R. E., Weiss, B. P., Maloof, A. C., Vali, H., Nash, C. Z., & Kirschvink, J. L. (2006). Chains, clumps, and strings; magnetofossil taphonomy with ferromagnetic resonance spectroscopy. *Earth and Planetary Science Letters, 247*(1-2), 10–25. https://doi.org/10.1016/j.epsl.2006.05.001

Larrasoaña, J. C., Liu, Q., Hu, P., Roberts, A. P., Mata, P., Civis, J., Sierro, F. J., & Pérez-Asensio, J. N. (2014). Paleomagnetic and paleoenvironmental implications of magnetofossil

occurrences in late miocene marine sediments from the guadalquivir basin, SW spain. *Frontiers in Microbiology*, *5*, 71–71. https://doi.org/10.3389/fmicb.2014.00071

Lascu, I., Banerjee, S. K., & Berquó, T. S. (2010). Quantifying the concentration of ferrimagnetic particles in sediments using rock magnetic methods. *Geochemistry, Geophysics, Geosystems*, *11*(8), Q08Z19. https://doi.org/10.1029/2010GC003182

Lascu, I., Harrison, R. J., Li, Y., Muraszko, J. R., Channell, J. E. T., Piotrowski, A. M., & Hodell, D. A. (2015). Magnetic unmixing of first-order reversal curve diagrams using principal component analysis. *Geochemistry, Geophysics, Geosystems, 16*(9), 2900–2915. https://doi. org/10.1002/2015GC005909

Lascu, I., & Plank, C. (2013). A new dimension to sediment magnetism: charting the spatial variability of magnetic properties across lake basins. *Global and Planetary Change*, *110*, 340–349. https://doi.org/10.1016/j.gloplacha.2013.03.013

Li, J., Ge, K., Pan, Y., Williams, W., Liu, Q., & Qin, H. (2013). A strong angular dependence of magnetic properties of magnetosome chains: Implications for rock magnetism and paleomagnetism. *Geochemistry, Geophysics, Geosystems*, *14*, 3887–3907. https://doi.org/10.1002/ggge.20228

Li, J., Wu, W., Liu, Q., & Pan, Y. (2012). Magnetic anisotropy, magnetostatic interaction and identification of magnetofossils. *Geochemistry, Geophysics, Geosystems*, *13*, Q10Z51. https://doi.org/10.1029/2012GC004384

Lin, W., & Pan, Y. (2009). Uncultivated magnetotactic cocci from yuandadu park in beijing, china. *Applied and Environmental Microbiology*, *75*(12), 4046–4052. https://doi.org/10.1128/AEM.00247-09

Lin, W., Paterson, G. A., Zhu, Q., Wang, Y., Kopylova, E., Li, Y., Knight, R., Bazylinski, D. A.,

Zhu, R., Kirschvink, J. L., & Pan, Y. (2017). Origin of microbial biomineralization and magnetotaxis during the archean. *Proceedings of the National Academy of Sciences, 114*(9), 2171–2176. https://doi.org/10.1073/pnas.1614654114

Lin, W., Zhang, W., Paterson, G. A., Zhu, Q., Zhao, X., Knight, R., Bazylinski, D. A., Roberts, A. P., & Pan, Y. (2020). Expanding magnetic organelle biogenesis in the domain bacteria. *Microbiome, 8*(1), 152–152. https://doi.org/10.1186/s40168-020-00931-9

Lin, W., Zhang, W., Zhao, X., Roberts, A. P., Paterson, G. A., Bazylinski, D. A., & Pan, Y. (2018). Genomic expansion of magnetotactic bacteria reveals an early common origin of magnetotaxis with lineage-specific evolution. *The ISME Journal, 12*(6), 1508–1519. https://doi.org/10.1038/s41396-018-0098-9

Ludwig, P., Egli, R., Bishop, S., Chernenko, V., Frederichs, T., Rugel, G., Merchel, S., & Orgeira, M. J. (2013). Characterization of primary and secondary magnetite in marine sediment by combining chemical and magnetic unmixing techniques. *Global and Planetary Change, 110*, 321–339. https://doi.org/10.1016/j.gloplacha.2013.08.018

Maher, B. A. (1988). Magnetic properties of some synthetic sub-micron magnetites. *Geophysical Journal International, 94*(1), 83–96. https://doi.org/10.1111/j.1365-246X.1988.tb03429.x

Mao, X., Egli, R., Petersen, N., Hanzlik, M., & Zhao, X. (2014). Magnetotaxis and acquisition of detrital remanent magnetization by magnetotactic bacteria in natural sediment: first experimental results and theory. *Geochemistry, Geophysics, Geosystems, 15*(1), 255–283. https://doi.org/10.10002/2013GC005034

McNeill, D. F., & Kirschvink, J. L. (1993). Early dolomitization of platform carbonates and the preservation of magnetic polarity. *Journal of Geophysical Research: Solid Earth, 98*(B5), 7977–7986. https://doi.org/10.1029/93JB00353

Moskowitz, B. M., Frankel, R. B., Flanders, P. J., Blakemore, R. P., & Schwartz, B. B. (1988). Magnetic properties of magnetotactic bacteria. *Journal of Magnetism and Magnetic Materials*, *73*(3), 273–288. https://doi.org/10.1016/0304-8853(88)90093-5

Nagy, L., Williams, W., Muxworthy, A. R., Fabian, K., Almeida, T. P., Conbhui, P. O., et al. (2017). Stability of equidimensional pseudo-single-domain magnetite over billion-year timescales. *Proceedings of the National Academy of Sciences of the United States of America*, *114*(39), 10356–10360. https://doi.org/10.1073/pnas.1708344114

Néel, L. (1949). Théorie du traînage magnétique des ferromagnétiques en grains fins avec applications aux terres cuites. *Annales de Géophysique*, *5*(2), 99–136.

Néel, L. (1955). Some theoretical aspects of rock-magnetism. *Advances in Physics*, *4*(14), 191–243. https://doi.org/10.1080/00018735500101204.

Newell, A. J. (2005). A high-precision model of first-order reversal curve (FORC) functions for single-domain ferromagnets with uniaxial anisotropy. *Geochemistry, Geophysics, Geosystems*, *6*(5), Q05010. https://doi.org/10.1029/2004GC000877

Ó Conbhuí, P., Williams, W., Fabian, K., Ridley, P., Nagy, L., & Muxworthy, A. R. (2018). MERRILL: Micromagnetic earth related robust interpreted language laboratory. *Geochemistry, Geophysics, Geosystems*, *19*, 1080–1106. https://doi.org/10.1002/2017GC007279

Orue, I., Marcano, L., Bender, P., A. García-Prieto, Valencia, S., Mawass, M. A., et al. (2018). Configuration of the magnetosome chain: a natural magnetic nanoarchitecture. *Nanoscale*, *10*(16), 7407–7419. https://doi.org/10.1039/C7NR08493E

Pan, Y., Petersen, N., Winklhofer, M., Davila, A. F., Liu, Q., Frederichs, T., Hanzlik, M., & Zhu, R. (2005). Rock magnetic properties of uncultured magnetotactic bacteria. *Earth and*

Planetary Science Letters, *237*(3), 311–325. https://doi.org/10.1016/j.epsl.2005.06.029

Paterson, G. A., Wang, Y., & Pan, Y. (2013). The fidelity of paleomagnetic records carried by magnetosome chains. *Earth and Planetary Science Letters*, *383*, 82–91. https://doi.org/10.1016/j.epsl.2013.09.031

Philipse, A. P., & Maas, D. (2002). Magnetic colloids from magnetotactic bacteria: chain formation and colloidal stability. *Langmuir*, *18*(25), 9977–9984. https://doi.org/10.1021/la0205811

Roberts, A. P. (2015). Magnetic mineral diagenesis. *Earth-Science Reviews*, *151*, 1–47. https://doi.org/10.1016/j.earscirev.2015.09.010

Roberts, A. P., Chang, L., Heslop, D., Florindo, F., & Larrasoaña, J. C. (2012). Searching for single domain magnetite in the "pseudo-single-domain" sedimentary haystack: implications of biogenic magnetite preservation for sediment magnetism and relative paleointensity determinations. *Journal of Geophysical Research*, *117*, B08104. https://doi.org/10.1029/2012JB009412

Roberts, A. P., Florindo, F., Chang, L., Heslop, D., Jovane, L., & Larrasoaña, J. C. (2013). Magnetic properties of pelagic marine carbonates. *Earth-Science Reviews*, *127*, 111–139. https://doi.org/10.1016/j.earscirev.2013.09.009

Roberts, A. P., Florindo, F., Villa, G., Chang, L., Jovane, L., Bohaty, S. M., et al. (2011). Magnetotactic bacterial abundance in pelagic marine environments is limited by organic carbon flux and availability of dissolved iron. *Earth and Planetary Science Letters*, *310*(3–4), 441–452. https://doi.org/10.1016/j.epsl.2011.08.011

Shcherbakov, V. P., Winklhofer, M., Hanzlik, M., & Petersen, N. (1997). Elastic stability of chains of magnetosomes in magnetotactic bacteria. *European Biophysics Journal*, *26*(4),

319–326. https://doi.org/10.1007/s002490050086

Tarduno, J. A., Tian, W., & Wilkison, S. (1998). Biogeochemical remanent magnetization in pelagic sediments of the western equatorial pacific ocean. *Geophysical Research Letters, 25*(21), 3987–3990. https://doi.org/10.1029/1998GL900079

Trelis (2021). (Version 2021.3) [computer software]. Coreform LLC. Retrieved from http://coreform.com

Yamazaki, T. (2012). Paleoposition of the Intertropical Convergence Zone in the eastern Pacific inferred from glacial-interglacial changes in terrigenous and biogenic magnetic mineral fractions. *Geology, 40*(2), 151–154. https://doi.org/10.1130/g32646.1

Yamazaki, T., & Kawahata, H. (1998). Organic carbon flux controls the morphology of magnetofossils in marine sediments. *Geology, 26*(12), 1064–1066. https://doi.org/10.1130/0091-7613(1998)026<1064:OCFCTM>2.3.CO;2

Yamazaki, T., & Yamamoto, Y. (2018). Relative paleointensity and inclination anomaly over the last 8 myr obtained from the integrated ocean drilling program site U1335 sediments in the eastern equatorial pacific. *Journal of Geophysical Research: Solid Earth, 123*(9), 7305–7320. https://doi.org/10.1029/2018JB016209

Zhao, X., Roberts, A. P., Heslop, D., Paterson, G. A., Li, Y., & Li, J. (2017). Magnetic domain state diagnosis using hysteresis reversal curves. *Journal of Geophysical Research: Solid Earth, 122*(7), 4767–4789. https://doi.org/10.1002/2016JB013683

Figure 1. Schematic diagram of geometries for modeled magnetosome chains. (a) A regular bending model, where the bending angle *b* represents the center angle corresponding to the regularly curved arc. (b) Morphological parameters of chains (i.e., *x*: length, *z*: width, *y*: height, *d*: space, *n*: number, and angle between adjacent particles). (c) A collapsed magnetosome chain model. (d) Generation process of the random-walk collapse model: (1) adding a new particle to the end of the chain with spacing *d*; (2) rotating the new particle by the collapse angle *c*, around the axis perpendicular to the plane formed by the existing and new particle; (3) rotating the new particle by a random angle around the axis parallel to the axis formed by the existing and new particle when it was first created (Harrison and Lascu, 2014).

Figure 2. Rock magnetic parameters as a function of bending/collapse angle: coercivity (B_c), coercivity of remanence (B_{cr}), and ratio of saturation remanence to saturation magnetization (M_{rs}/M_s) for bending (a, c, e) and collapse (b, d, f) models.

Figure 3. Simulated hysteresis loop and switching mode of domain states for a strongly bending magnetosome chain (40 nm, cuboctahedra, loose spacing, b = 300°). Blue arrows highlight the domain direction. Black arrow represents the direction of the external magnetic field. Small arrows within particles show magnetic moments and were colored by helicity.

Figure 4. Simulated hysteresis loop and switching mode of domain states for a strongly collapsed magnetosome chain (i.e., 40 nm, cuboctahedra, loose spacing, c = 70°). Other symbols are the same as in Figure 3.

Figure 5. Saturation remanent states for selected modeled magnetosome chains. Yellow surfaces mark vortex cores. Other symbols are the same as in Figure 3.

Figure 6. Simulated FORC diagrams of four typical 40 nm magnetosome chains: (a) straight-chain; (b) strongly bent chain ($b = 300°$); (3) medium collapse model ($c = 30°$); (4) strong

collapse model ($c = 60°$). FORC diagrams were processed using Forcot (Berndt & Chang, 2019).

Figure 7. Simulated pDRM intensity change of a single chain relative to straight chain (a, b), average normalized pDRM intensity (pDRM/SIRM) change relative to straight chain (c, d) as a function of bending/collapse angle. Black and gray lines represent analytical calculations of magnetic moment rotation. Color lines are determined from micromagnetic calculations.

Figure 8. Selected pDRM states of modeled magnetosome chains. Other symbols are the same as in Figure 3.

Figure 9. Calculated minimum energy paths of the straight chain model (b = 0°) and ring-shaped chain model (b = 324°) at 500 ℃ using the NEB method. Red line indicates the calculated original path between the two endpoints. Green and blue lines represent the two new paths recalculated using the NEB method by splitting the original path at the intermediate minimum. Blue arrows highlight the domain direction.

Figure 10. Calculated energy paths of two collapsed chain models (c = 30° and 70°) at 520 ℃. Purple and brown lines represent two new paths recalculated by splitting again the first splitting path at the intermediate minimum again. Other legends are the same as Figure 9.

Figure 11. Evaluated blocking temperatures of four magnetosome chain models by polynomial fitting relaxation time. Green scatters represent relaxation times calculated by the NEB method. Orange lines were obtained by polynomial fitting. Gray dotted lines indicate the relaxation time (τ = 100 s) corresponding to the blocking temperature.

Figure 12. Néel diagram (M_{rs}/M_s versus B_c; Néel, 1955) of modeled hysteresis parameters in this study and experimental data of MTB (Jovane et al., 2012; Li et al., 2012; Lin & Pan, 2009; Moskowitz et al., 1988; Pan et al., 2005) and magnetofossil-rich sediments (Chang et al., 2018;

Ludwig et al., 2013). Gray arrow indicates the direction of increasing collapse angle. Numbers along the data lines represent collapse angle.

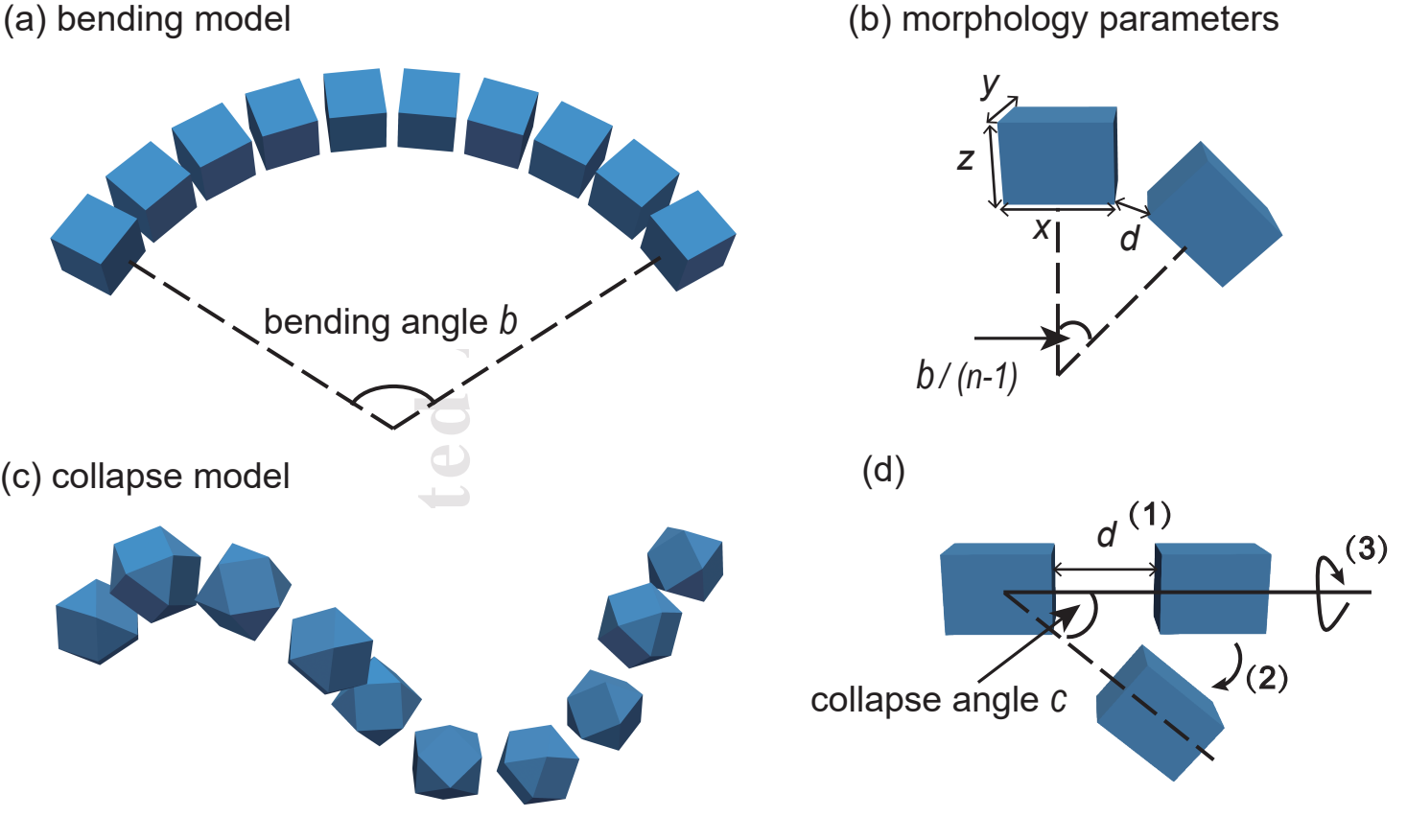
(a) bending model
bending angle b
(b) morphology parameters
y
z
x
d
b / (n-1)
(c) collapse model
(d)
d
(1)
(2)
(3)
collapse angle c

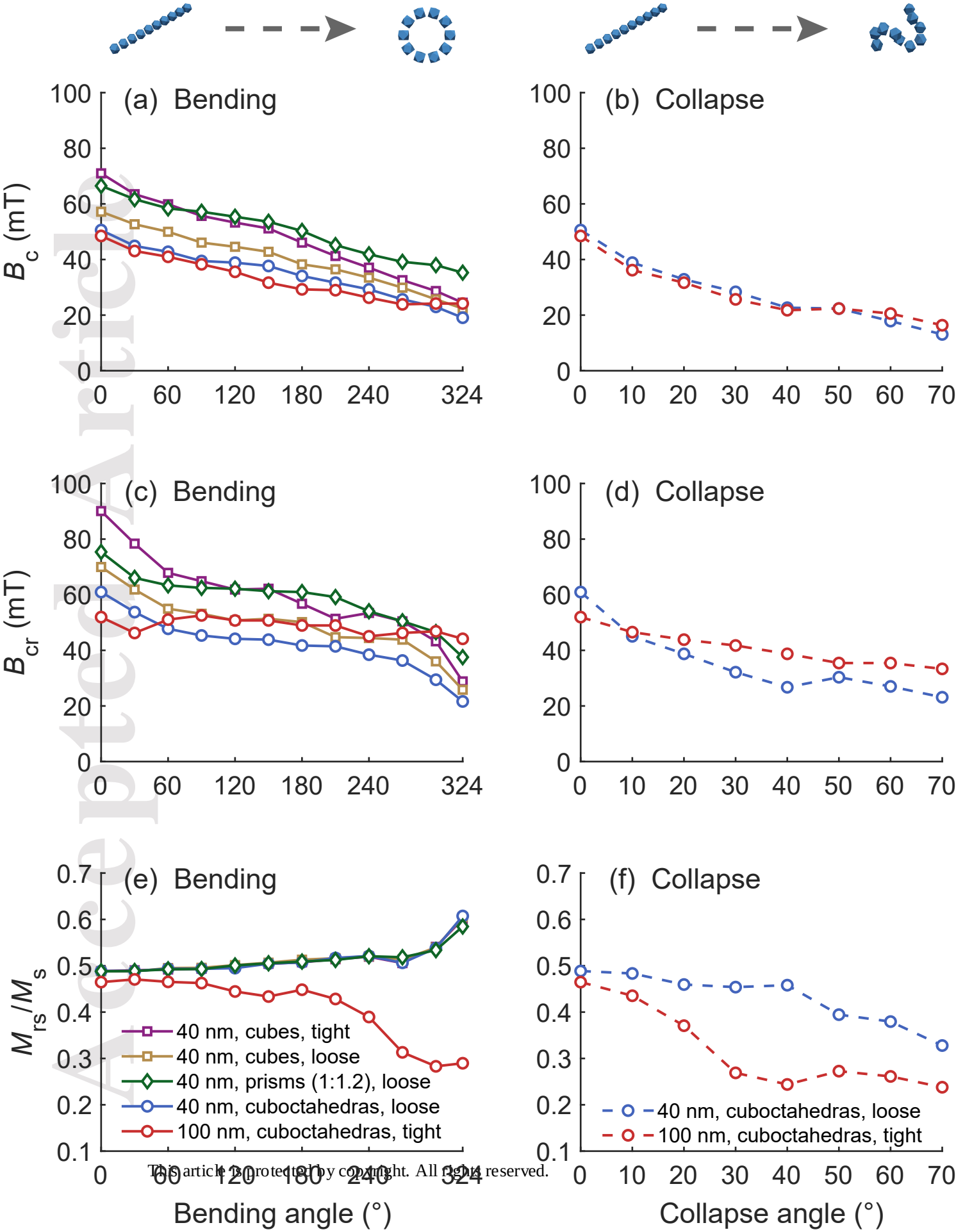

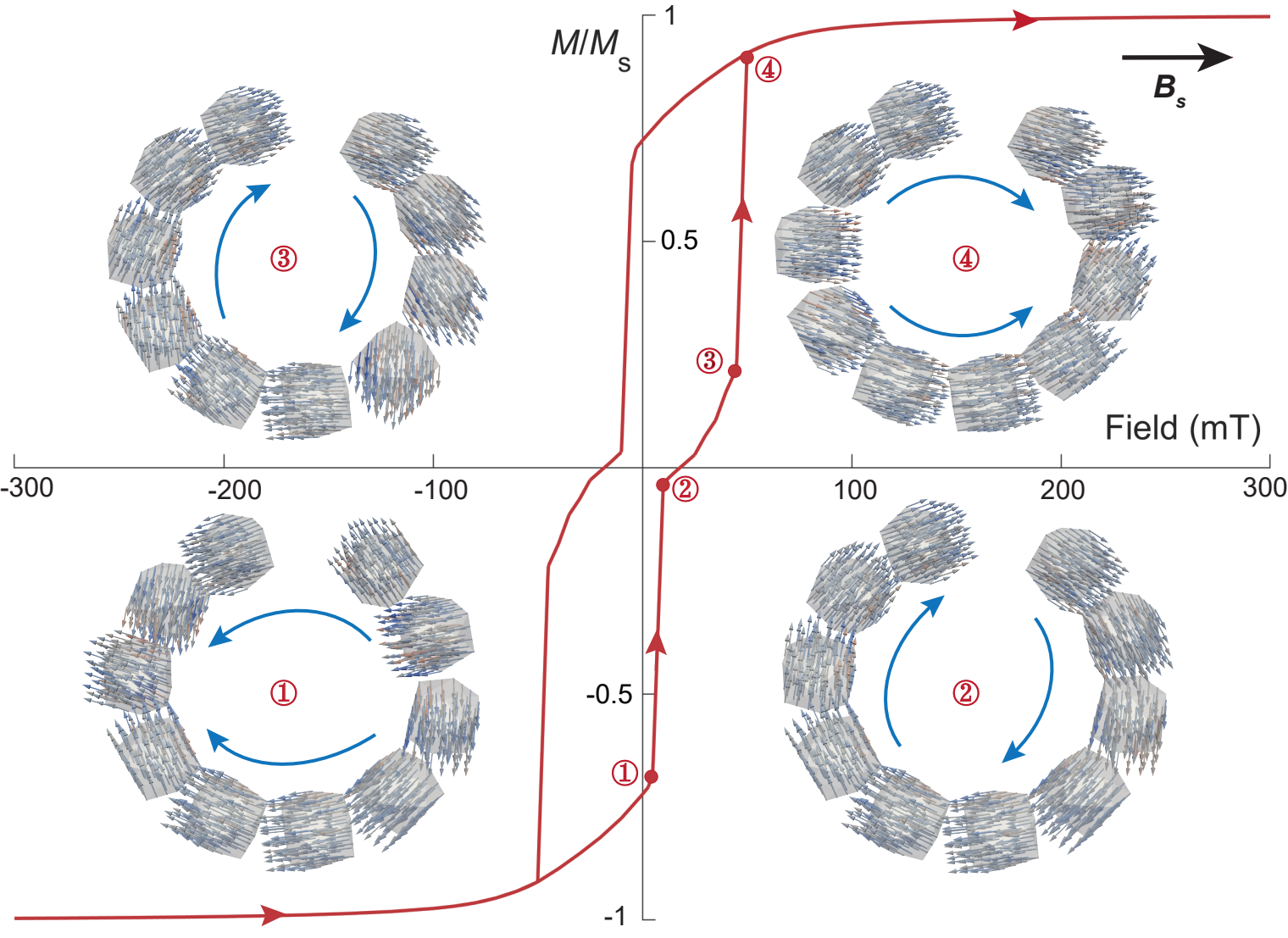
M/M_S
1
0.5
-0.5
-1
-300
-200
-100
100
200
300
Field (mT)
B_s
①
②
③
④

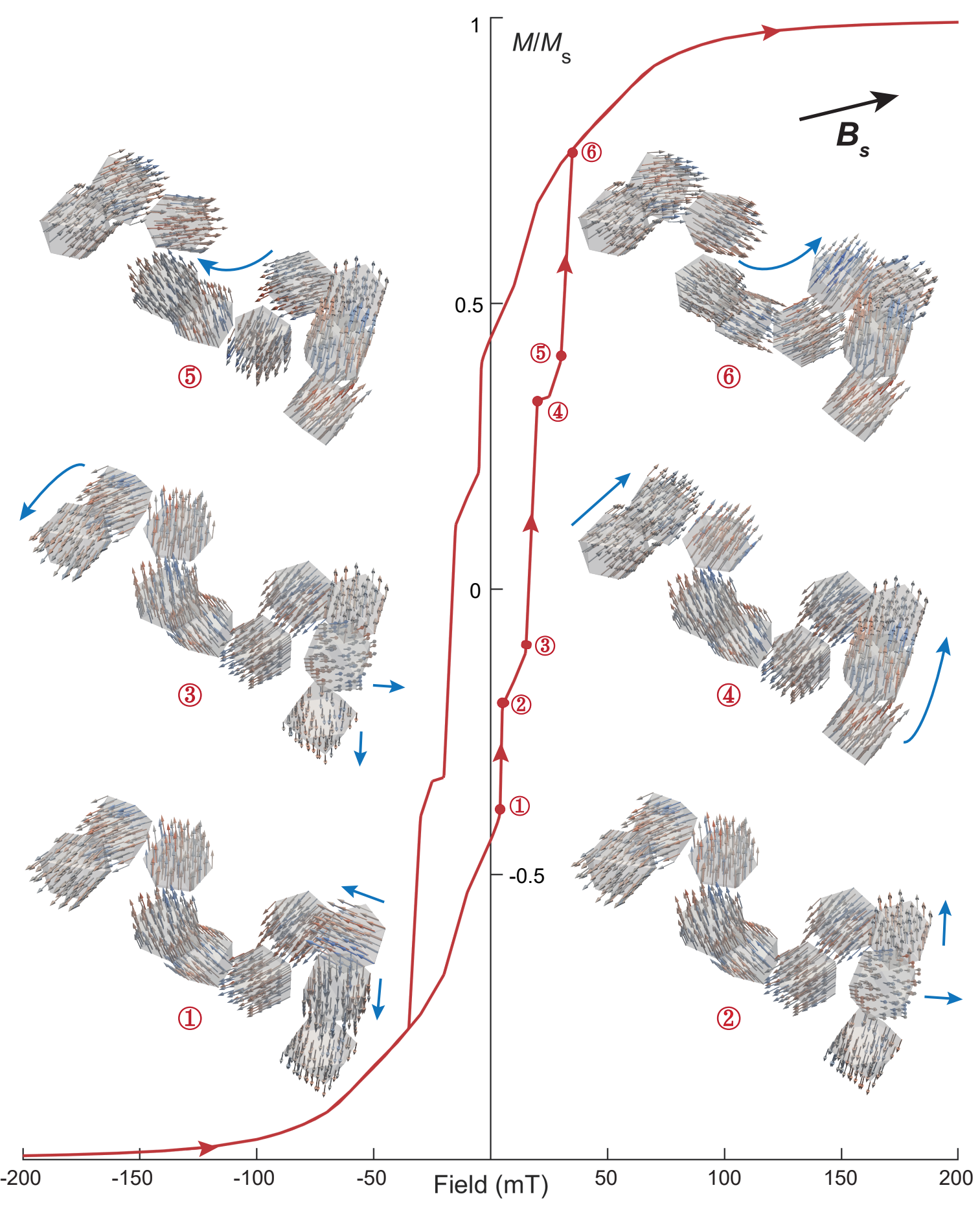
M/M_s
B_s
1
0.5
0
-0.5
-200
-150
-100
-50
50
100
150
200
Field (mT)
①
②
③
④
⑤
⑥

(a) bending angle = 30°
40 nm, cuboctahera, loose

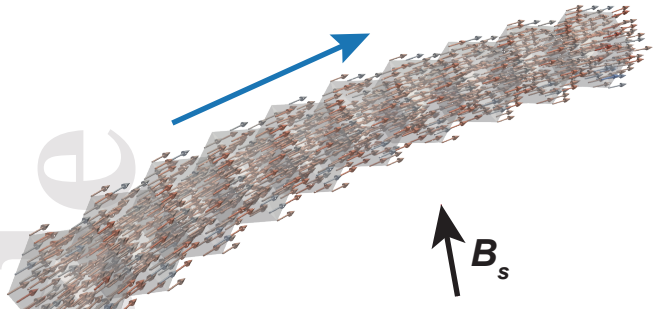

(b) bending angle = 180°
40 nm, cuboctahera, loose

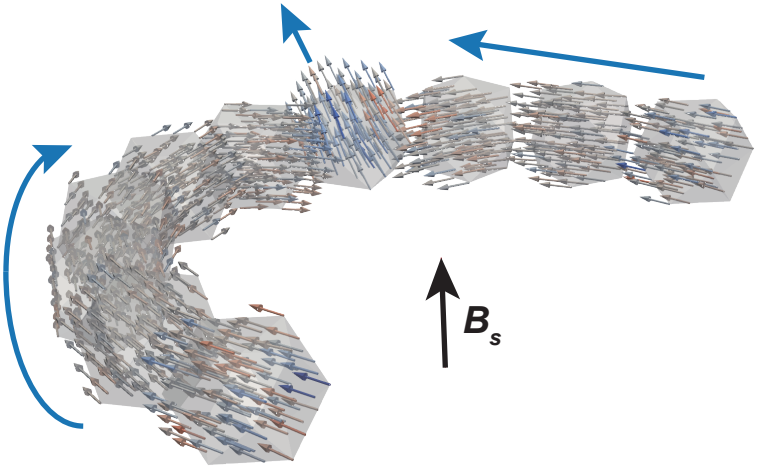

(c) bending angle = 30°
100 nm, cuboctahera, tight

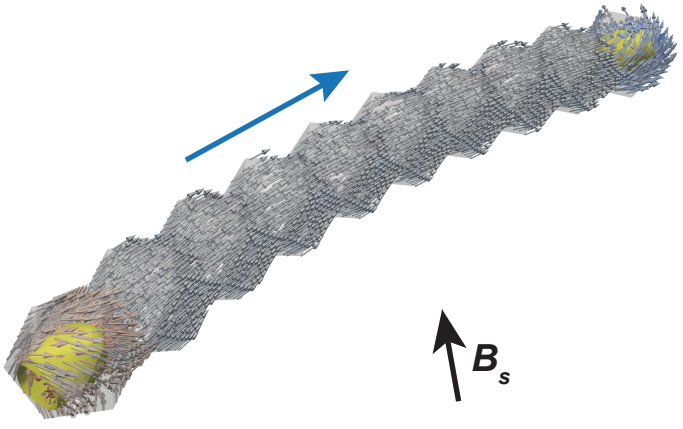

(d) bending angle = 300°
100 nm, cuboctahera, tight

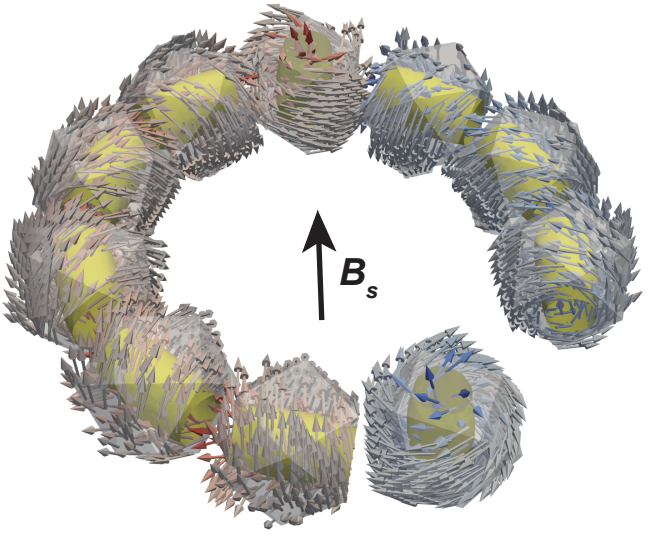

(e) collapse angle = 50°
40 nm, cuboctahera, loose

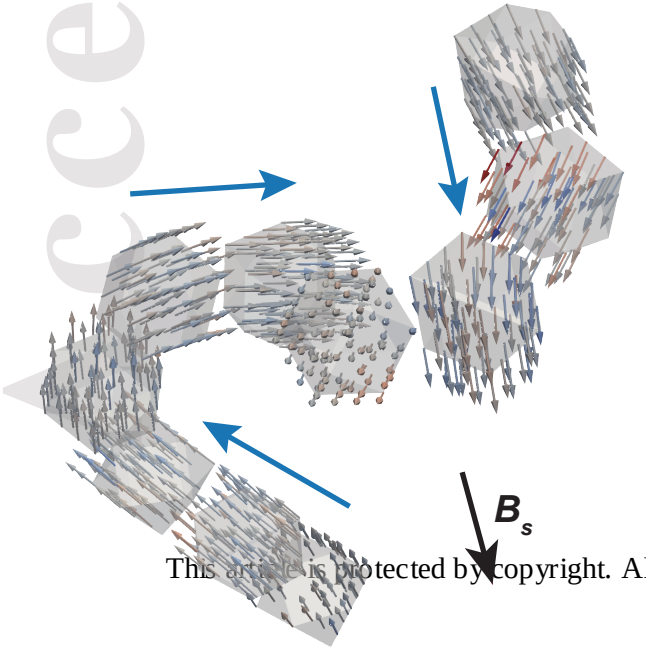

(f) collapse angle = 50°
100 nm, cuboctahera, tight

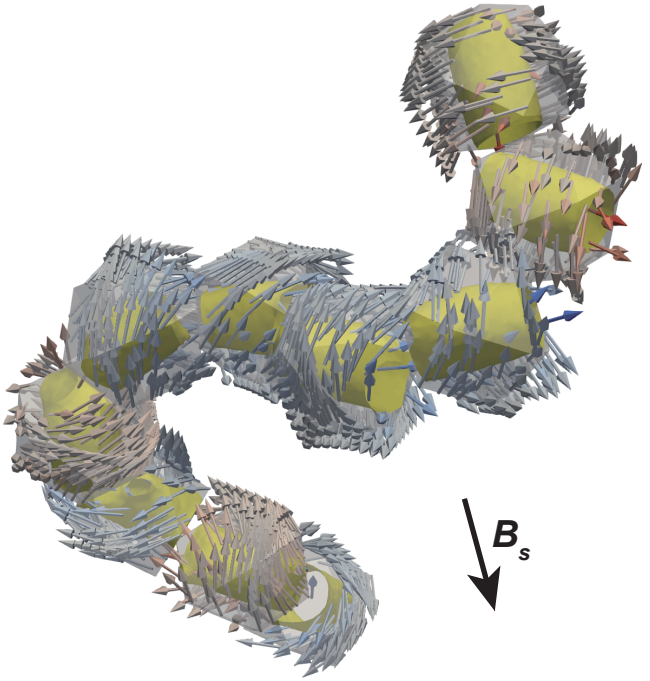

(a)

SF=3.9

(b)

SF=3.9

(c)

SF=2.9

(d)

SF=3.2

B_u [mT]

B_c [mT]

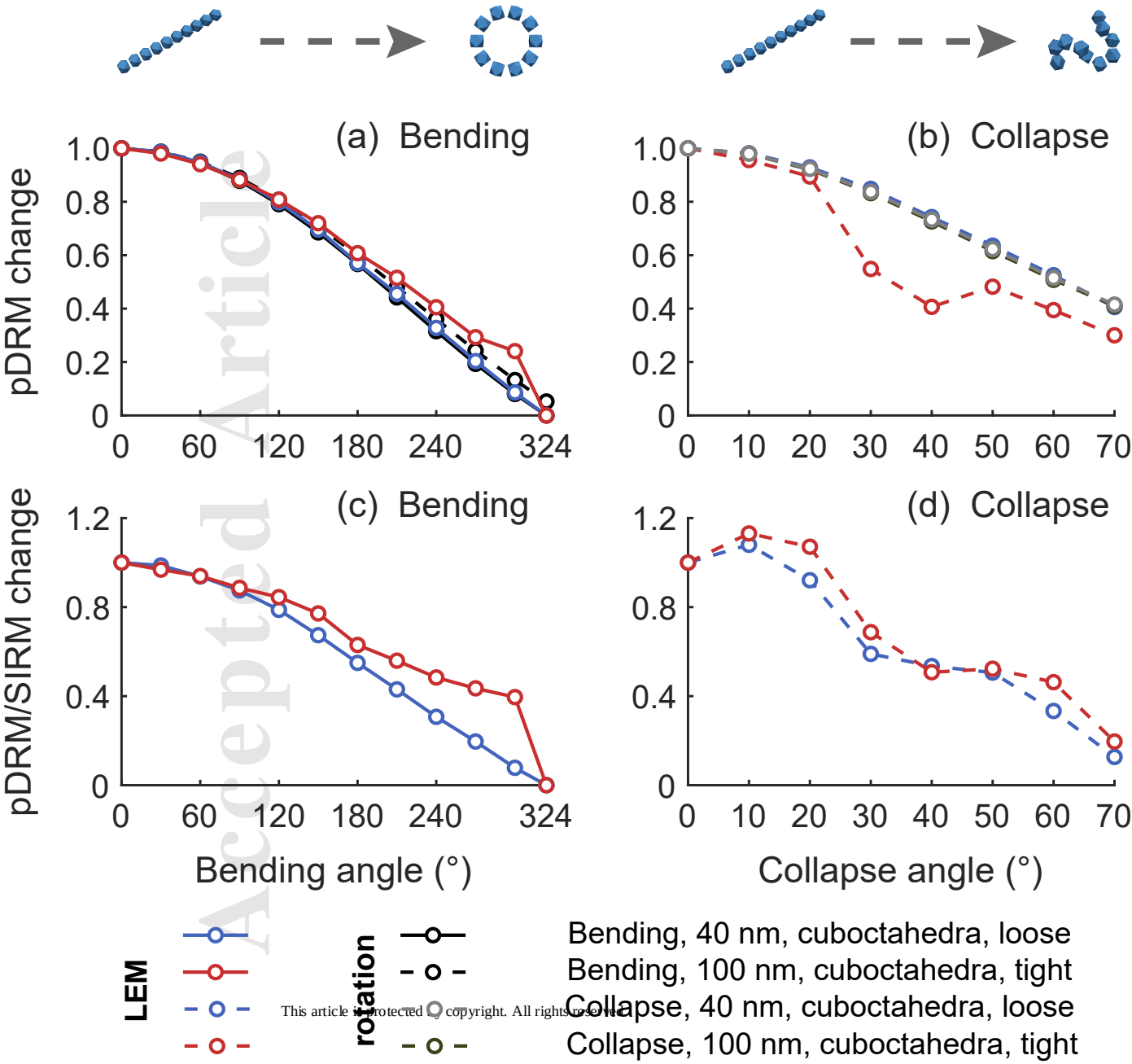

(a) bending angle = 0°
40 nm, cuboctahera, loose

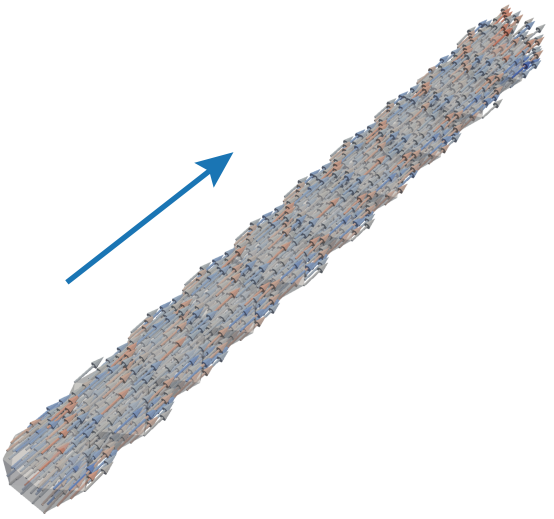

(b) bending angle = 0°
100 nm, cuboctahera, tight

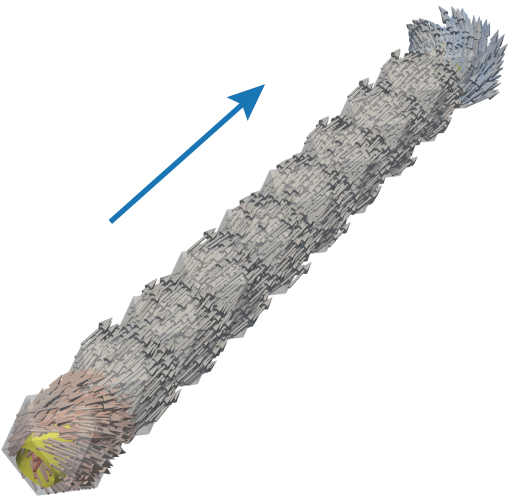

(c) collapse angle = 60°
40 nm, cuboctahera, loose

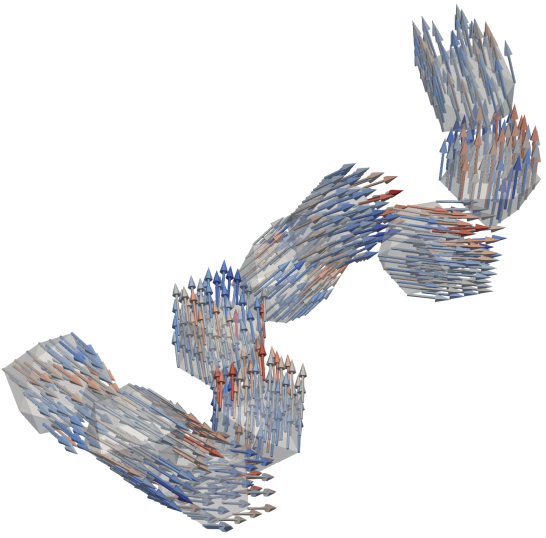

(d) collapse angle = 60°
100 nm, cuboctahera, tight

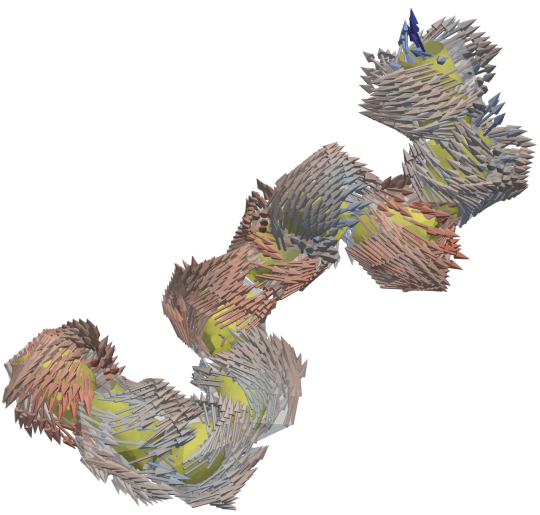

(e) bending angle = 300°
40 nm, cuboctahera, loose

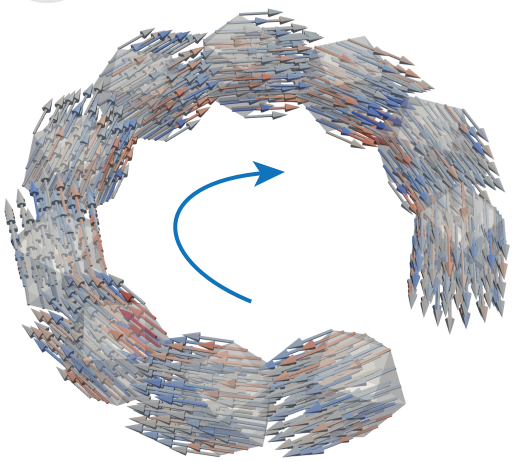

(f) bending angle = 300°
100 nm, cuboctahera, tight

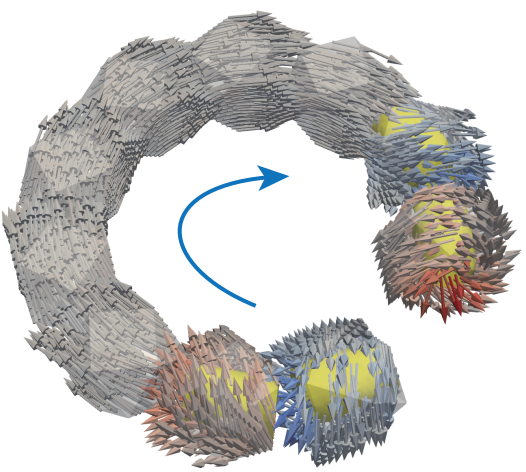

(a) bending angle = 0°, 40 nm, cuboctahera, loose, T = 500 °C

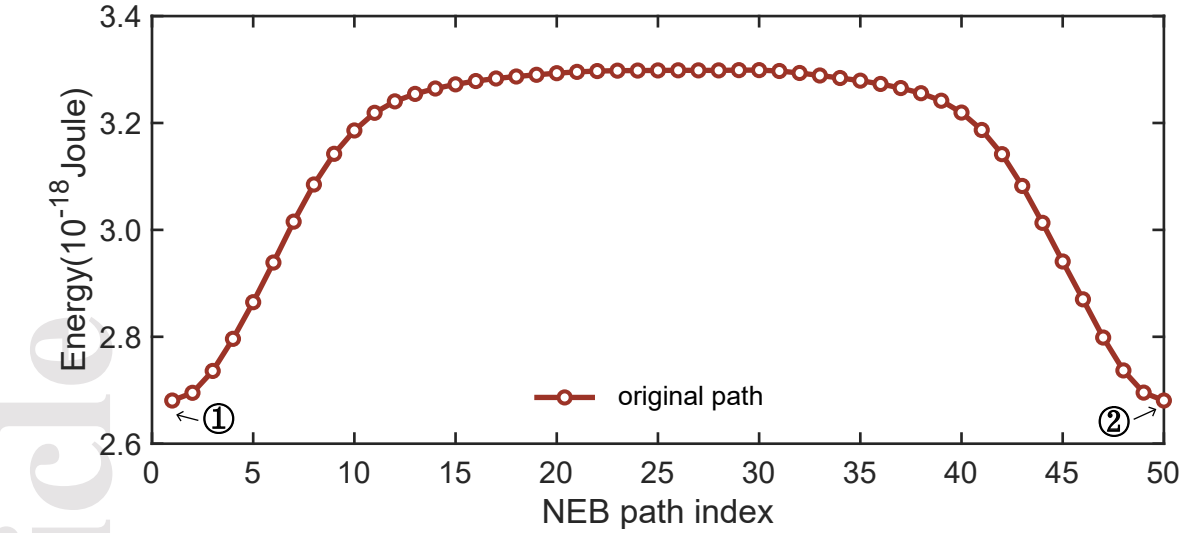

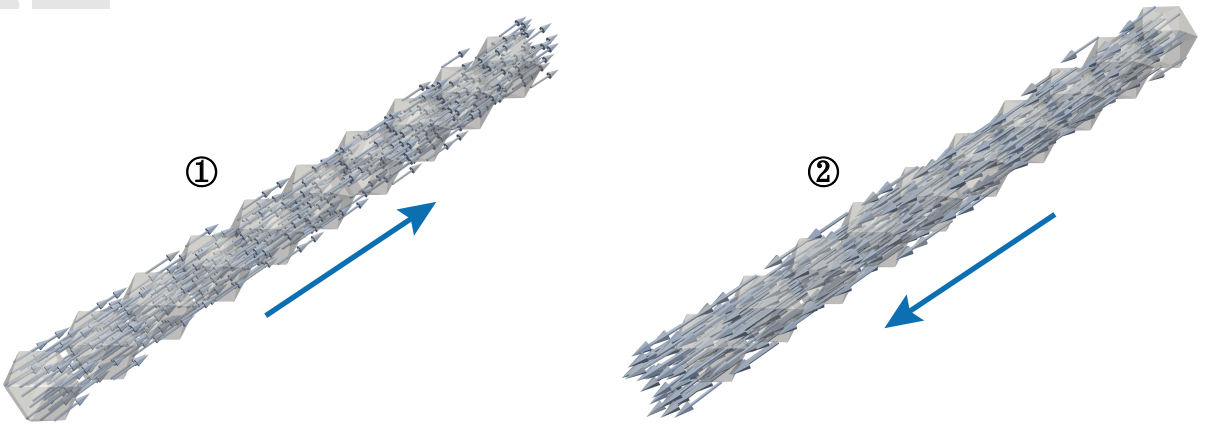

(b) bending angle = 324°, 40 nm, cuboctahera, loose, T = 500 °C

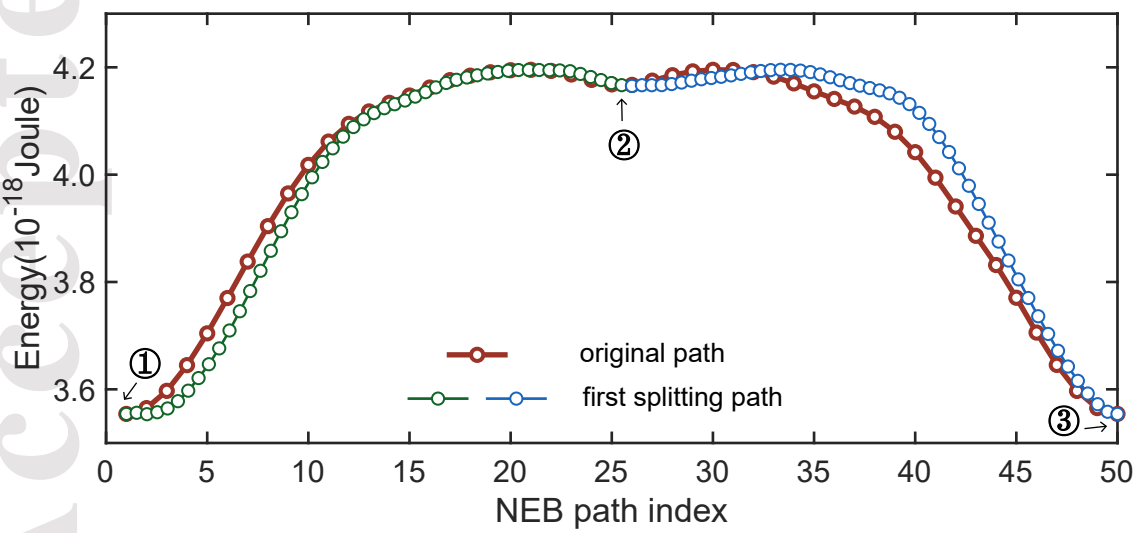

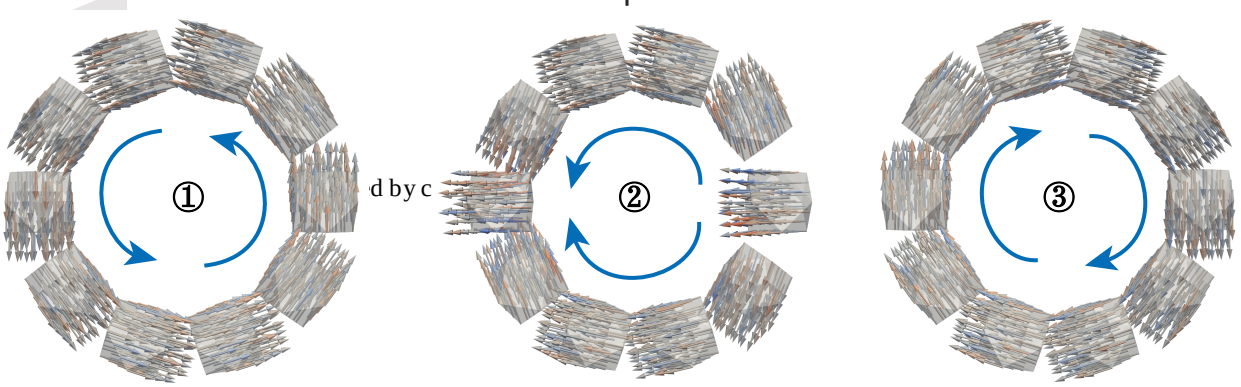

(a) collapse angle = 30°, 40 nm, cuboctahera, loose

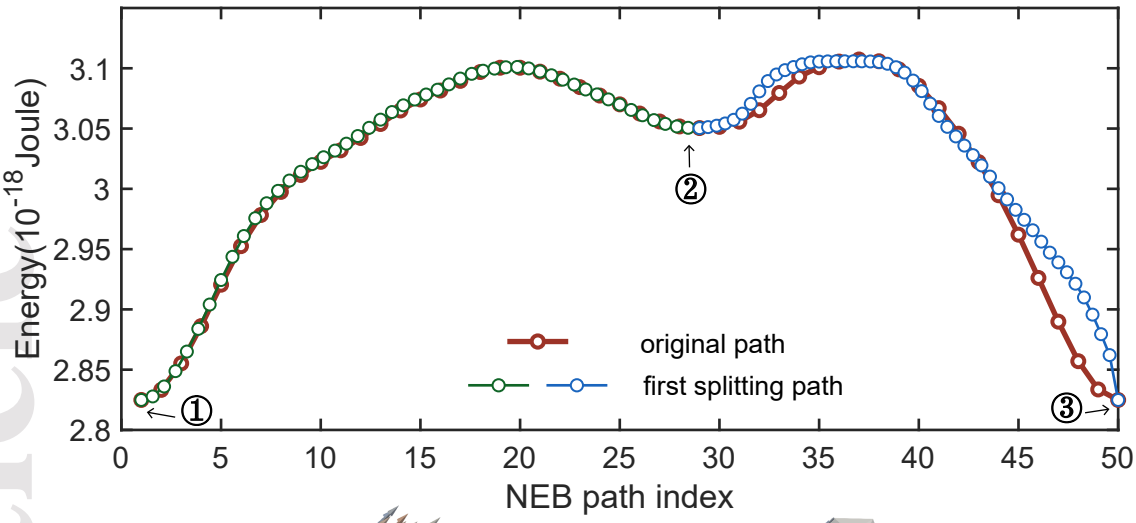

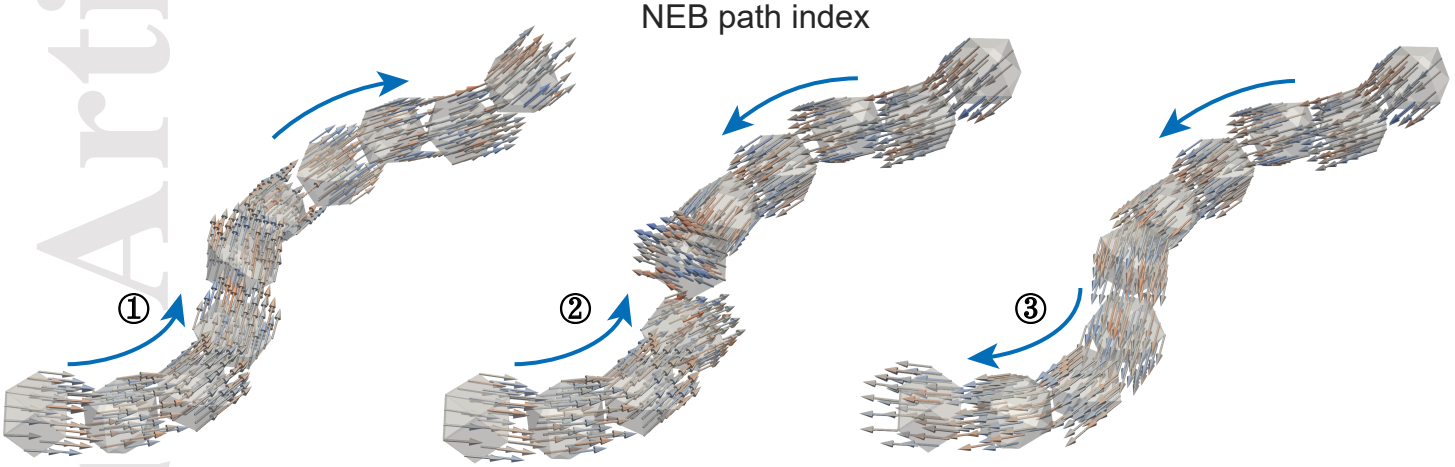

(b) collapse angle = 70°, 40 nm, cuboctahera, loose